![CSH PROTOCOLS] Cold Spring Harbor Protocols

Spectral Methods for Functional Brain Imaging

David Kleinfeld and Partha P. Mitra

Email Alerting Service	Receive free email alerts when new articles cite this article - **click here.**
Subject Categories	Browse articles on similar topics from *Cold Spring Harbor Protocols.* Image Analysis (102 articles) Imaging for Neuroscience (263 articles)

Spectral Methods for Functional Brain Imaging

David Kleinfeld and Partha P. Mitra

Dynamic functional imaging experiments typically generate large, multivariate data sets that contain considerable spatial and temporal complexity. The goal of this introduction is to present signal-processing techniques that allow the underlying spatiotemporal structure to be readily distilled and that also enable signal versus noise contributions to be separated.

INTRODUCTION

We present multivariate signal-processing techniques that help reveal the spatiotemporal structure of optical imaging data and also allow signal versus noise contributions to be separated. These techniques typically assume that the underlying activity may be modeled as stationary stochastic processes over short analysis windows; that is, the statistics of the activity do not change during the analysis period. This requires selection of an appropriate temporal window for the analysis, which can be checked in a self-consistent manner.

The following worked examples are provided that serve to show the utility and implementation of these spectral methods.

1. Deduction of rhythmic components of the dilation and constriction of a cortical penetrating arteriole in rat to illustrate basic frequency-domain concepts.
2. Deduction of synaptic connectivity between neurons in the leech swim network to emphasize the notions of spectral coherence and the associated confidence limits.
3. The denoising of imaging data in the study of calcium waves in brain slice to introduce the concept of singular value decomposition (SVD) in the time domain and to illustrate the notion of space–time correlation in multisite measurements.
4. The delineation of wave phenomena in turtle visual cortex to illustrate spectrograms, along with the concept of SVD in the frequency domain to determine the dominant patterns of spatial coherence in a frequency localized manner.

Much of our exposition involves spectral analysis. Why work in the frequency domain? First, many physiological phenomena have rhythmic components, ranging from electrical rhythms in the brain to visceral functions like breathing and heartbeat. The time series of these phenomena may appear very complicated, yet the representation in the frequency domain may be relatively simple and readily connected with underlying physiological processes. Second, the calculation of confidence intervals requires that the number of degrees of freedom are known. Determining this number is complicated in the time domain, where all but white noise processes lead to correlation between neighboring data points. In contrast, counting the number of degrees of freedom is readily established

Cite this introduction as *Cold Spring Harb Protoc*; doi:10.1101/pdb.top081075

in the frequency domain, as neighboring frequency bins are uncorrelated under stationarity assumptions. Our emphasis is on the explanation and applications of signal processing methods and not on scientific questions per se.

Some relevant signal processing texts include Papoulis (1962), Ahmed and Rao (1975), and Percival and Walden (1993). The latter book includes sections on multitaper spectral analysis methods, developed originally by Thomson (1982) and used extensively in our analysis. Applications of modern signal-processing methods to problems from neuroscience can be found in the book by Mitra and Bokil (2008) and in numerous reviews (Mitra and Pesaran 1998; Mitra et al. 1999; Pesaran et al. 2005; Kleinfeld 2008). Our notation follows that in Mitra and Bokil (2008).

BACKGROUND

The process of data collection involves sampling a voltage or current so that the signals are represented as an ordered set of points, called a time series, that are collected at a regular time interval. Let us denote the sampled time series as $V(t)$, the sampling time interval as Δt, and the length of sampling as T. In spectral analysis, one reexpresses this time series in the frequency domain by decomposing $V(t)$ into a weighted sum of sinusoids. We must first understand the range of frequencies that may be represented in the data.

The lowest resolvable frequency interval is given by the inverse of the length of the analysis window and is denoted by the Rayleigh frequency, $\Delta f_{\mathrm{Rayleigh}} = 1/T$. In multitaper spectral analysis, the resolution bandwidth is typically denoted as $2\Delta f$, where Δf is an adjustable parameter. The resolution bandwidth $2\Delta f$ is also parameterized by the dimensionless product, p, of the half-bandwidth Δf and the length of the window T, such that

$$\Delta f\, T = p, \tag{1}$$

with $p \geq 1$.

Sampling a continuous signal at discrete time intervals will in general lead to a loss of signal. However, there is an important class of signals, the so-called band-limited signals whose spectral transforms vanish outside of a frequency range whose highest frequency is denoted B. For this case, the signal can be perfectly reconstructed from discrete samples at uniform intervals Δt, as long as the sampling interval satisfies $\Delta t < 1/(2B)$. An alternative way of representing this criterion is to define the so-called Nyquist frequency, $f_{\mathrm{Nyquist}} = 1/(2\Delta t)$. Then the criterion for perfect reconstruction of the original band-limited signal from sampled data becomes $f_{\mathrm{Nyquist}} > B$.

Neural signals are not naturally band-limited, although physiological mechanisms such as the membrane time constant of neurons provide natural cutoff frequencies. It is customary to low-pass filter the original analog signal so that it becomes effectively band-limited and the Nyquist criterion may be applied. Typically, f_{Nyquist} is chosen to be significantly greater than B, which is called "over-sampling." However, if $\Delta t > 1/(2B)$, the sampling is not sufficiently rapid and signals at frequencies greater than B are reflected back, or "aliased," into the sampled interval that ranges from 0 to f_{Nyquist}. For example, a signal at $1.4 \times f_{\mathrm{Nyquist}}$ is aliased to appear at $0.6 \times f_{\mathrm{Nyquist}}$. The experimentally imposed low-pass filters to prevent aliasing are often called "antialiasing filters." Such filtering is not always possible and aliasing cannot always be avoided.

The discrete Fourier transform of a data segment is defined by

$$\tilde{V}(f) = \frac{1}{\sqrt{T}} \sum_{t=\Delta t}^{T} \Delta t\; e^{-2\pi i f t} V(t). \tag{2}$$

Qualitatively, the time series $V(t)$ is projected against all possible sinusoids, indexed by frequency f, to form a set of weights $\tilde{V}(f)$. An immediate complication is that the finite extent of our data is equivalent to multiplying an infinite data series with a square pulse of width T. The effect of such a

window on the Fourier transform is to produce oscillations for each estimate of $\tilde{V}(f)$ that extend into neighboring frequency bands (Fig. 1A,B). This is known as leakage, and is minimized by multiplying the time series with a function of time, denoted a taper, that smoothes the sharp edges of the pulse. A half-sine taper offers improvement, but a special function devised specifically to minimize leakage and known as a Slepian taper is optimal. The cost of reduced leakage is decreased spectral resolution
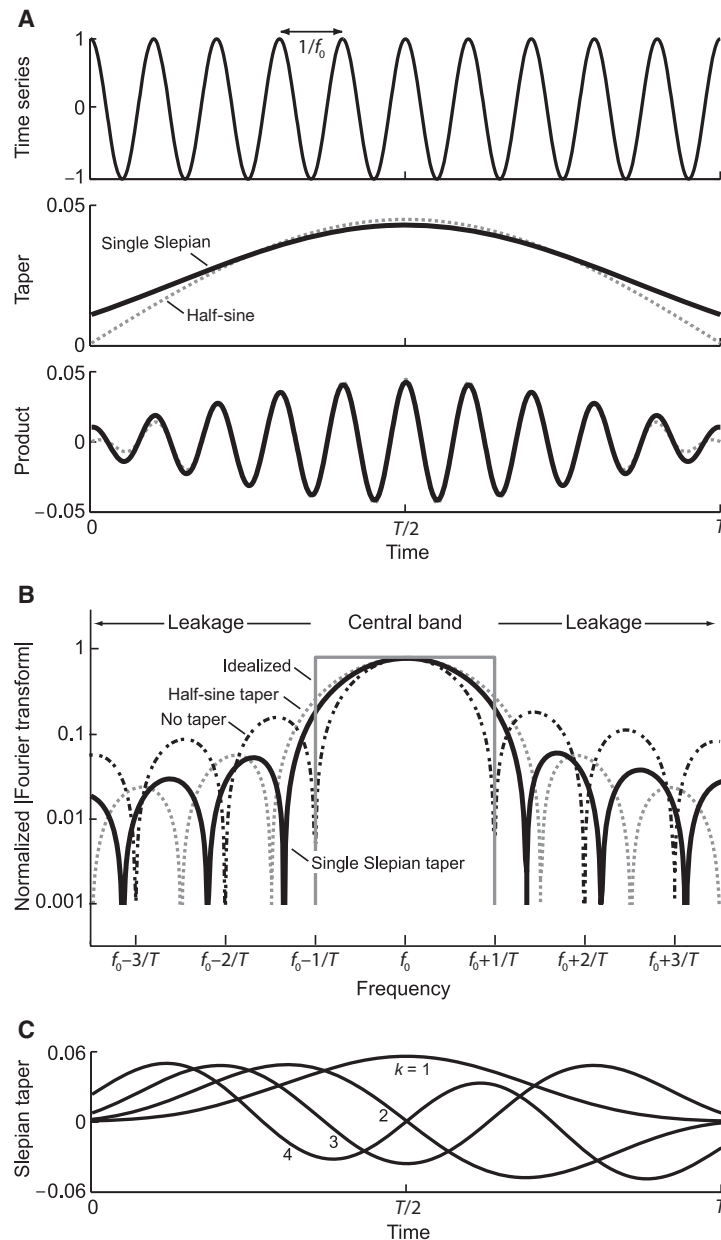
FIGURE 1. Basics of Fourier transforms and tapers. (*A*) Example of the process of tapering data. *Top* panel shows the time series of a sine wave with center frequency $f_0 = T/10$. *Middle* panel shows a half-sine taper, defined as $\sin\{\pi t/T\}$, and a single Slepian taper with $p = 1$ and $K = 1$; the norm of both functions are set to 1. *Bottom* panel shows the products of the tapers and the time series. (*B*) Magnitude of the Fourier transforms of the untapered data, the data tapered with a single taper, and the data tapered with a single Slepian taper. Also shown is the "ideal" representation with power only in the interval $[-1/T, 1/T]$ surrounding the center frequency. For the case of no taper, the transform is $\tilde{V}(f) \sim \sin\{\pi(f - f_0)/T\}/[\pi(f - f_0)/T]$, and the first zero is at $f = \pm 1/T$ relative to f_0, whereas for the case of the half-sine taper, $\tilde{V}(f) \sim \cos\{\pi(f - f_0)/T\}/\{[1 - 2(f - f_0)/T]^2\}$, and the first zero is at $f = \pm 3/(2T)$ relative to f_0. There is no analytical expression for the transform of the Slepian taper. (*C*) The family of four Slepian tapers, $w^{(k)}(t)$, for the choice $p = 2.5$.

through an increase in the resolution bandwidth (Fig. 1B). There are considerable advantages to computing a family of independent estimates, $\tilde{V}^{(k)}(f)$, rather than a single estimate, and in weighting the data with a set of orthonormal Slepian tapers to form this family (Fig. 1C). We denote each taper in the set by $w^{(k)}(t)$ and compute the estimates

$$\tilde{V}^{(k)}(f) = \frac{1}{\sqrt{T}} \sum_{t=\Delta t}^{T} \Delta t \ e^{-2\pi ft} w^{(k)}(t) V(t).$$ (3)

The maximum number of tapers, denoted K, that supports this minimization, and which is used throughout our presentation, is

$$K = 2p - 1.$$ (4)

The lower spectral resolution, or equivalently a larger resolution bandwidth, is offset by a greater number of spectral estimates $\tilde{V}^{(k)}(f)$. The increase in number of independent estimates minimizes the distortion of the value in one frequency band by the value in a neighboring band and thus improves the statistical reliability of quantities that depend on the Fourier transform of the original signal.

Numerical processing of sampled data requires that we work in dimensionless units. We normalize time by the sample time, Δt, so that the number of data points in the time series is given by $N \equiv T/\Delta t$. We further normalize the resolution bandwidth by the sample time, Δt, and define the unitless half-bandwidth $W \equiv \Delta t \Delta f$. Then the time–frequency product $T \Delta f = p$ is transformed to

$$NW = p.$$ (5)

Given sampled data,

$$\tilde{V}^{(k)}(f) = \frac{1}{\sqrt{N}} \sum_{t=1}^{N} e^{-i2f\pi t} w_t^{(k)} V_t,$$ (6)

where time is now an index that runs from 1 to N in steps of 1 rather than a discrete variable that runs from 0 to T in steps of Δt, whereas frequency runs from $-1/2$ to $+1/2$ in steps of $1/N$ (Table 1).

Implementation of the algorithms can be in any programming environment, but the use of the MatLab-based programming environment along with packaged routines in Chronux (http://www.chronux.org) is particularly convenient.

CASE ONE: SPECTRAL POWER

As a means of introducing spectral estimation, we analyze the rhythms that give rise to motion of the wall of a penetrating arteriole that sources blood to cortex (Fig. 2A). These arterioles are gateways that transfer blood from the surface of cortex to the underlying microvasculature (Nishimura et al. 2007).

TABLE 1. Relation of laboratory and computational units

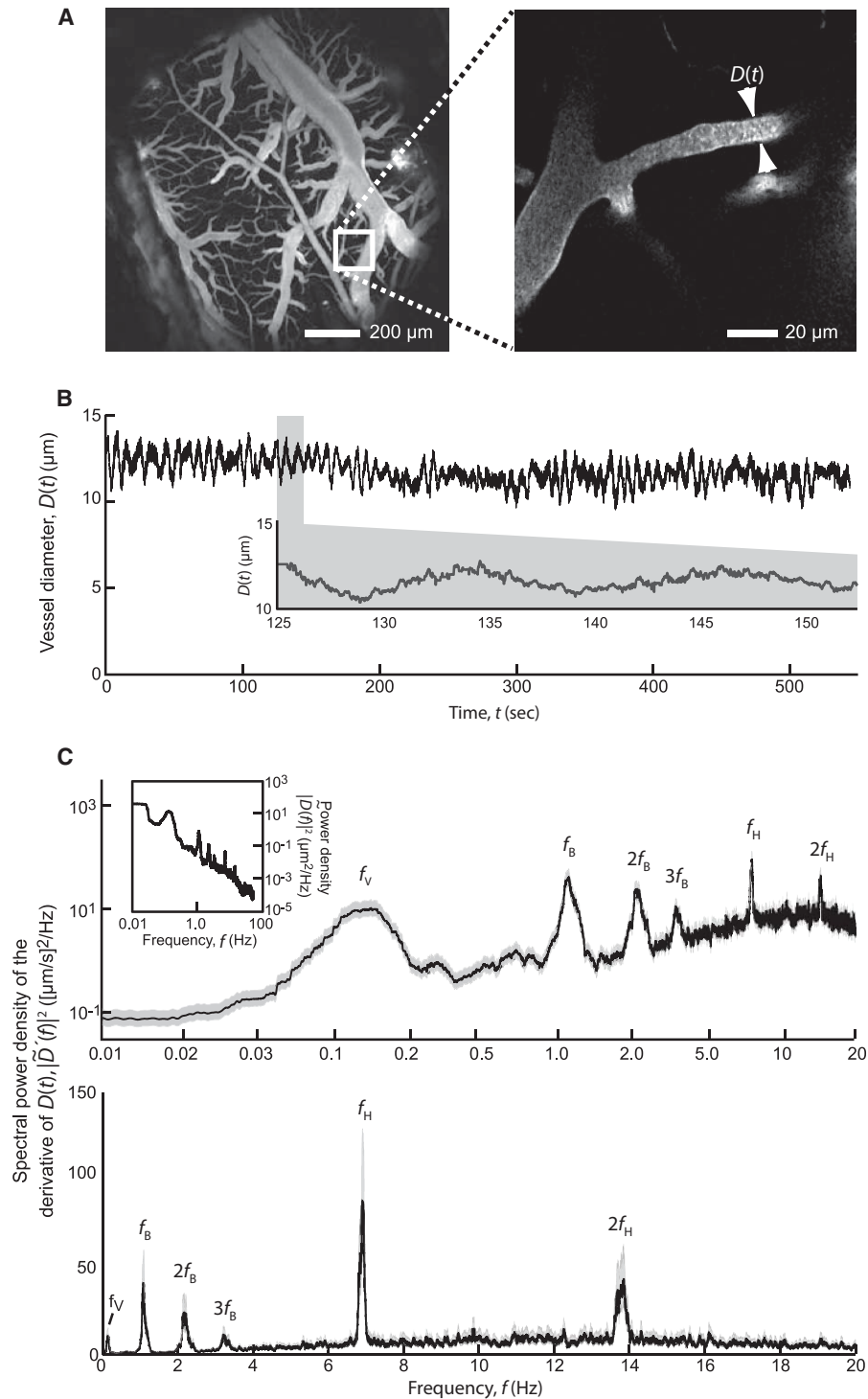| Quantity		Units	
Name	Description	Sampled data	Computational
Record length	Longest time	T	N
Sample time	Shortest time	$\Delta t = T/N$	1
Resolution half-bandwidth	Lowest frequency	$\Delta f = p/T$	$W = p/N$
Nyquist frequency ($f_{Nyquist}$)	Highest frequency	$1/2\Delta t = N/2T$	1/2
Temporal range		$[\Delta t, T]$	$[1, N]$
Spectral range		$[-N/2T, N/2T]$	$[-1/2, 1/2]$
Time-bandwidth product (p)	$p \geq 1$	$T \bullet \Delta f$	$N \bullet W$

D. Kleinfeld and P.P. Mitra

FIGURE 2. Analysis of the intrinsic motion of the diameter of a penetrating arteriole from rat. (*A*) Two-photon line-scan data through the center of a penetrating vessel over parietal cortex was obtained as described (Shih et al. 2009); $f_{Nyquist} = 500$ Hz. (*B*) Time series of the diameter as a function of time, as derived from the line-scan data as described (Devor et al. 2007) ($T = 540$ sec). The *inset* shows an expanded region to highlight the multiplicity of rhythmic events present in the signal. (*C*) Spectrum (Equations 8 and 9 with $p = 24$) of the time derivative of the diameter, $D'(t)$ (Equation 11) plotted on log–log (*top*) and linear–linear (*bottom*) axes. The gray bands encompass the 95% confidence bands (Equations 13–16) and appear symmetric on a log scale (*top*) but asymmetric on the linear scale (*bottom*). The frequencies are labeled f_V for vasomotion, f_B for breathing, and f_H for heartbeat. The *inset* in the *top* figure shows the spectrum of the diameter $D(t)$; note the steep, $\sim 1/f^2$ trend that is removed by taking the spectrum of $D'(t)$ (AY Shih, unpubl.).

Past work has established that isolated arterioles can generate myographic activity in the 0.1-Hz range (Osol and Halpern 1988), similar to that seen in vivo by noninvasive imaging techniques of brain tissue (Mayhew et al. 1996) and two-photon imaging of capillaries (Kleinfeld et al. 1998). Here we look at the relative contribution of vasomotion, as well as breathing and heart rate, to penetrating vessels.

The raw signal is the diameter of the vessel, denoted $D(t)$ (Fig. 2B). The mean value is removed to give

$$\delta D_t = D_t - \frac{1}{N}\sum_{t=1}^{N} D_t. \tag{7}$$

Our goal is to understand the spectral content of this signal—with confidence limits! The Fourier transform of this signal, with respect to the kth taper, is (Equation 6)

$$\delta\tilde{D}^{(k)}(f) = \frac{1}{\sqrt{N}}\sum_{t=1}^{N} e^{-i2\pi ft} w_t^{(k)} \delta D_t, \tag{8}$$

where, as noted previously (Equation 3), $w^{(k)}(t)$ is the kth Slepian taper, whose length is also T. We compute the spectral power density, denoted $\tilde{S}(f)$, with units of distance^2/frequency, in terms of an average over the index of tapers, that is,

$$\tilde{S}(f) \equiv \frac{1}{K}\sum_{k=1}^{K} \left|\delta\tilde{D}^{(k)}(f)\right|^2, \tag{9}$$

where $\left|\delta\tilde{D}^{(k)}(f)\right|^2 = \delta\tilde{D}^{(k)}(f)[\delta\tilde{D}^{(k)}(f)]^*$; we further average over all trials if appropriate. Note that the "$1/\sqrt{N}$" normalization satisfies Parseval's theorem, that is,

$$\sum_{f=0}^{f_{Nyquist}} \tilde{S}(f) = \frac{1}{N}\sum_{t=1}^{N} D_t^2. \tag{10}$$

The spectrum in this example has strong features, yet has a trend to decrease as roughly $1/f^2$ that tends to obscure the peaks (inset in Fig. 2C). We remove the trend by computing the spectrum of the temporal derivative of δD_t,

$$\delta D_t' = \frac{\delta D_{t+1} - \delta D_t}{\Delta t}, \tag{11}$$

as a means to flatten or "prewhiten" the spectrum. We now observe a multitude of peaks on a relatively flat background (Fig. 2C). A broad peak is centered at 0.2 Hz and corresponds to vasomotion. A sharper peak near 1 Hz corresponds to breathing; the nonsinusoidal shape of variations in diameter caused by breathing leads to the presence of second and third harmonics. Finally, a sharp peak at 7 Hz corresponds to heart rate and also includes a harmonic. No additional peaks are observed beyond the second harmonic of breathing. Note that the resolution half-bandwidth was chosen to be $\Delta f = 0.03$ Hz ($p = 16$), which is narrower than the low-frequency band.

The next issue is the calculation of confidence intervals so that the uncertainty in the power at each peak may be established and the statistical significance of each peak may be assessed. Confidence limits may be estimated analytically for various asymptotic limits. However, the confidence intervals may also be estimated directly by a jackknife, where we compute the standard error in terms of "delete-one" means (Thomson and Chave 1991). In this procedure, we exploit the multiple estimates of the spectral power density and calculate K different mean spectra in which one term is left out, that is,

$$\tilde{S}^{(n)}(f) \equiv \frac{1}{K-1} \sum_{\substack{k=1 \\ k \neq n}}^{K} \left| \delta \tilde{D}^{(k)}(f) \right|^2. \tag{12}$$

Estimating the standard error of the spectral power density requires an extra step because spectral amplitudes are defined on the interval $[0, \infty)$, whereas Gaussian variables exist on the full interval $(-\infty, \infty)$. Taking the logarithm leads to variables defined over the full interval; thus we transform the delete-one estimates, $S^{(n)}(f)$, according to

$$g\left\{\tilde{S}^{(n)}(f)\right\} \equiv \ln\left\{\tilde{S}^{(n)}(f)\right\} \tag{13}$$

or

$$\tilde{S}^{(n)}(f) = e^{g\left\{\tilde{S}^{(n)}(f)\right\}}. \tag{14}$$

The mean of the transformed variable is

$$\tilde{\mu}(f) \equiv \frac{1}{K} \sum_{k=1}^{K} g\left\{\tilde{S}^{(n)}(f)\right\} \tag{15}$$

and the standard error is

$$\tilde{\sigma}(f) = \sqrt{\frac{K-1}{K} \sum_{n=1}^{K} \left[g\left\{\tilde{S}^{(n)}(f)\right\} - \mu(f) \right]^2}. \tag{16}$$

The 95% confidence limit for the transformed spectral density is given by $2\tilde{\sigma}(f)$, so that one visualizes $\tilde{S}(f)$ by plotting the mean value of $\tilde{S}(f)$ (i.e., $e^{\tilde{\mu}(f)}$) along with the lower and upper bounds (i.e., $e^{\tilde{\mu}(f)-2\tilde{\sigma}(f)}$ and $e^{\tilde{\mu}(f)+2\tilde{\sigma}(f)}$, respectively). The confidence bands are symmetric about the mean when spectral power is plotted on a logarithmic scale (upper trace in Fig. 2C) rather than on a linear scale (lower trace in Fig. 2C).

CASE TWO: COHERENCE BETWEEN TWO SIGNALS

To introduce coherence, a measure of the tracking of one rhythmic signal by another, we consider the use of optical imaging to determine potential pair-wise connections between neurons (Cacciatore et al. 1999). We focus on imaging data taken from the ventral surface of a leech ganglion and seek to identify cells in the ganglion that receive monosynaptic input from neuron Tr2 in the head (Fig. 3A). This cell functions as a toggle for the swim rhythm in these animals. Rather than serially impale each of the roughly 400 cells in the ganglion and look for postsynaptic currents induced by driving Tr2, a parallel strategy was adopted (Taylor et al. 2003). The cells in the ganglion were stained with a voltage-sensitive dye (Fig. 3B), which transforms changes in membrane potential into changes in the intensity of fluorescent light. The emitted light from all cells is detected with a charge-coupled device (Fig. 3B), from which time series for the change in fluorescence are calculated for each neuron in the field (Fig. 3C). Presynaptic cell Tr2 was stimulated with a periodic signal, at frequency f_{Drive}, with the assumption that candidate postsynaptic followers of Tr2 would fire with the same periodicity (Fig. 3D). The phase of the coherence relative to the drive depends on the sign of the synapse, propagation delays, and filtering by postsynaptic processes.

The coherence between the response of each cell and the drive, a complex function denoted $\tilde{C}_i(f)$, was calculated over the time period of the stimulus. We denote the measured time series of the optical signals as $O_i(t)$ and the reference drive signal as $R(t)$. The spectral coherence is defined as
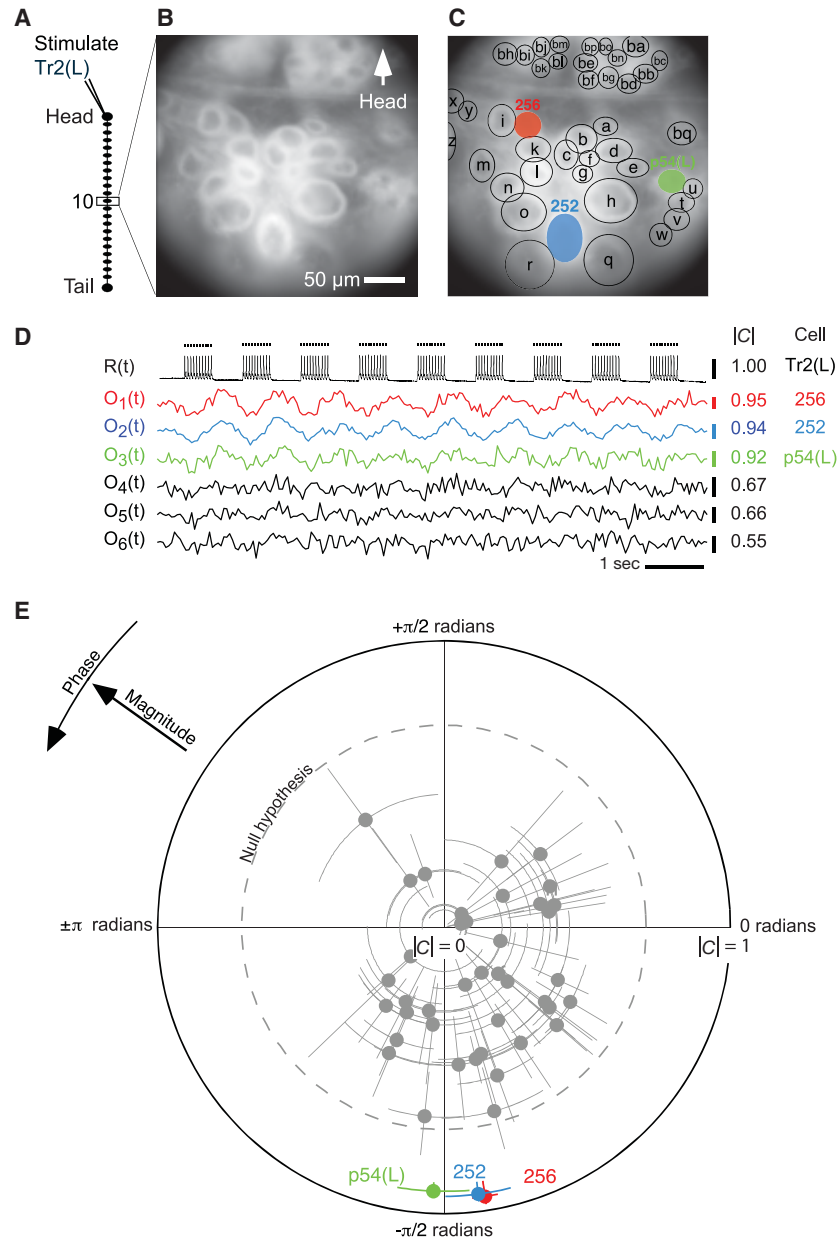
FIGURE 3. Analysis of voltage-sensitive dye imaging experiments to find followers of Tr2. (*A*) Cartoon of the leech nerve cord; input to Tr2 forms the drive signal $U(t)$. (*B*) Fluorescence image of ganglion 10 stained with dye. (*C*) Ellipses drawn to encompass individual cells and define regions whose pixel outputs were averaged to form the optical signals $V_i(t)$. (*D*) Simultaneous electrical recording of Tr2 (i.e., $U(t)$), and optical recordings from six of the cells shown in panel C ($T = 9$ sec) (i.e., $V_1(t)$ through $V_6(t)$), along with $\left|\tilde{C}_i(f_{\text{Drive}})\right|$ (Equation 17 with $p = 6$). (*E*) Polar plot of $\tilde{C}_i(f_{\text{Drive}})$ between each optical recording and the cell Tr2 electrical recording for all 43 cells in panel C. The dashed line indicates the $\alpha = 0.001$ threshold for significance (Equations 24 and 25); error bars one standard error (Equations 18–25). (Modified from Taylor et al. 2003.)

$$\tilde{C}_i(f) = \frac{\dfrac{1}{K}\sum_{k=1}^{K}\tilde{O}_i^{(k)}(f)\left[\tilde{R}_i^{(k)}(f)\right]^{*}}{\sqrt{\left(\dfrac{1}{K}\sum_{k=1}^{K}\left|\tilde{O}_i^{(k)}(f)\right|^2\right)\left(\dfrac{1}{K}\sum_{k=1}^{K}\left|\tilde{R}_i^{(k)}(f)\right|^2\right)}}. \tag{17}$$

D. Kleinfeld and P.P. Mitra

To calculate the standard errors for the coherence estimates, we again use the jackknife (Thomson and Chave 1991) and compute delete-one averages of coherence, denoted by $\tilde{C}_i^{(n)}(f)$, where n is the index of the deleted taper, that is,

$$\tilde{C}_i^{(n)}(f) = \frac{\frac{1}{K-1}\sum_{\substack{k=1 \\ k \neq n}}^{K} \tilde{O}_i^{(k)}(f)\left[\tilde{R}_i^{(k)}(f)\right]^*}{\sqrt{\left(\frac{1}{K-1}\sum_{\substack{k=1 \\ k \neq n}}^{K}\left|\tilde{O}_i^{(k)}(f)\right|^2\right)\left(\frac{1}{K-1}\sum_{\substack{k=1 \\ k \neq n}}^{K}\left|\tilde{R}_i^{(k)}(f)\right|^2\right)}}. \tag{18}$$

Estimating the standard error of the magnitude of $\tilde{C}_i(f)$, as with the case for the spectral power, requires an extra step because $\left|\tilde{C}_i(f)\right|$ is defined on the interval $[0, 1]$, whereas Gaussian variables exist on $(-\infty, \infty)$. The mean value of the magnitude of the coherence for each postsynaptic cell (i.e., $\left|\tilde{C}_i(f)\right|$) and the delete-one estimates, $\left|\tilde{C}_i^{(n)}(f)\right|$, are replaced with the transformed values

$$g\left\{\left|\tilde{C}_i^{(n)}(f)\right|\right\} = \ln\left(\frac{\left|\tilde{C}_i^{(n)}(f)\right|^2}{1 - \left|\tilde{C}_i^{(n)}(f)\right|^2}\right) \tag{19}$$

or

$$\left|\tilde{C}_i^{(n)}(f)\right| = \frac{1}{\sqrt{1 + e^{-g\left\{\left|\tilde{C}_i^{(n)}(f)\right|\right\}}}}. \tag{20}$$

The means of the transformed variables are

$$\tilde{\mu}_{i;\text{Mag}}(f) = \frac{1}{K}\sum_{n=1}^{K} g\left\{\tilde{C}_i^{(n)}(f)\right\} \tag{21}$$

and their standard errors are

$$\tilde{\sigma}_{i;\text{Mag}}(f) = \sqrt{\frac{K-1}{K}\sum_{n=1}^{K}\left|g\left\{\tilde{C}_i^{(n)}(f)\right\} - \tilde{\mu}_{i;\text{Mag}}(f)\right|^2}. \tag{22}$$

The 95% confidence interval for $\left|\tilde{C}_i(f)\right|$ corresponds to values within the interval

$$\left[\sqrt[-1]{1 + e^{-\left(\tilde{\mu}_{i;\text{Mag}} - 2\tilde{\sigma}_{i;\text{Mag}}\right)}},\ \sqrt[-1]{1 + e^{-\left(\tilde{\mu}_{i;\text{Mag}} + 2\tilde{\sigma}_{i;\text{Mag}}\right)}}\right].$$

For completeness, an alternate transformation for computing the variance is

$$g\left\{\tilde{C}_i(f)\right\} = \tanh^{-1}\left\{\tilde{C}_i(f)\right\}.$$

We now consider an estimate of the standard deviation of the phase of $\left|\tilde{C}_i(f)\right|$. Conceptually, the idea is to compute the variation in the relative directions of the delete-one unit vectors (i.e.,

Cite this introduction as *Cold Spring Harb Protoc*; doi:10.1101/pdb.top081075

$\tilde{C}_i(f)/\left|\tilde{C}_i(f)\right|$). The standard error is computed as

$$\tilde{\sigma}_{i;\text{Phase}}(f) = \sqrt{2\frac{K-1}{K}\left(K - \left|\sum_{n=1}^{K}\frac{\tilde{C}_i^{(n)}(f)}{\left|\tilde{C}_i^{(n)}(f)\right|}\right|\right)}. \tag{23}$$

Our interest is in the values of $\tilde{C}_i(f)$ for $f = f_{\text{Drive}}$ and the confidence limits for this value. We choose the resolution bandwidth so that the estimate of $\left|\tilde{C}_i(f_{\text{Drive}})\right|$ is kept separate from that of the harmonic $\left|\tilde{C}_i(2f_{\text{Drive}})\right|$; the choice $\Delta f = 0.4f_{\text{Drive}}$ works well. We graph the magnitude and phase of $\tilde{C}_i(f_{\text{Drive}})$ for all neurons, along with the confidence intervals, on a polar plot (Fig. 3E).

Finally, we consider whether the coherence of a given cell at f_{Drive} is significantly >0 (i.e., larger than one would expect by chance from a signal with no coherence) as a means to select candidate postsynaptic targets of Tr2. We compared the estimate for each value of $\tilde{C}_i(f_{\text{Drive}})$ with the null distribution for the magnitude of the coherence, which exceeds

$$\left|\tilde{C}_i(f_{\text{Drive}})\right| = \sqrt{1 - \alpha^{1/(K-1)}} \tag{24}$$

only in a fraction α of the trials (Hannan 1970; Jarvis and Mitra 2001). We used $\alpha = 0.001$ in our experiments to avoid false positives. We also calculated the multiple comparisons α level for each trial, given by

$$\alpha_{\text{multi}} = 1 - (1 - \alpha)^N, \tag{25}$$

where N is the number of cells in the functional image, and verified that it did not exceed $\alpha_{\text{multi}} = 0.05$ on any trial (Fig. 3E).

The result of the above procedure was the discovery of three postsynaptic targets of cell Tr2, two of which were functionally unidentified neurons (Taylor et al. 2003).

CASE THREE: SPACE–TIME SINGULAR-VALUE DECOMPOSITION AND DENOISING

A common issue in the analysis of optical imaging data is the need to remove "fast" noise, that is, fluctuations in intensity that occur on a pixel-by-pixel and frame-by-frame basis. The idea is that the imaging data contains features that are highly correlated in space, such as underlying cell bodies, processes, etc., and highly correlated in time, such as long-lasting responses. The imaging data may thus be viewed as a space–time matrix of random numbers (i.e., the fast noise) with added correlated structure. The goal is to separate the fast, uncorrelated noise from the raw data so that a compressed image file with only the correlated signals remains (Fig. 4A,B shows single frames; for the complete movies, see Movies 1 and 2 online at http://cshprotocols.cshlp.org). With this model in mind, we focus on the case of intracellular Ca^{2+} oscillations in an organotypic culture of rat cortex, which contains both neurons and glia. All cells were loaded with a fluorescence-based calcium indicator, and spontaneous activity in the preparation was imaged with a fast-framing ($\Delta t = 2$ msec), low-resolution (100×100 pixels) confocal microscope (Fig. 4A).

Imaging data is in the form of a three-dimensional array of intensities, denoted $V(x, y, t)$. We consider expressing the spatial location in terms of a pixel index, so that each $(x, y) \rightarrow s$ and the data is now in the form of a space–time matrix (i.e., $V(s, t)$). This matrix may be decomposed into the outer product of functions of pixel index with functions of time. Specifically,

$$V(s, t) = \sum_{n=1}^{\text{rank}\{V\}} \lambda_n F_n(s) G_n(t), \tag{26}$$
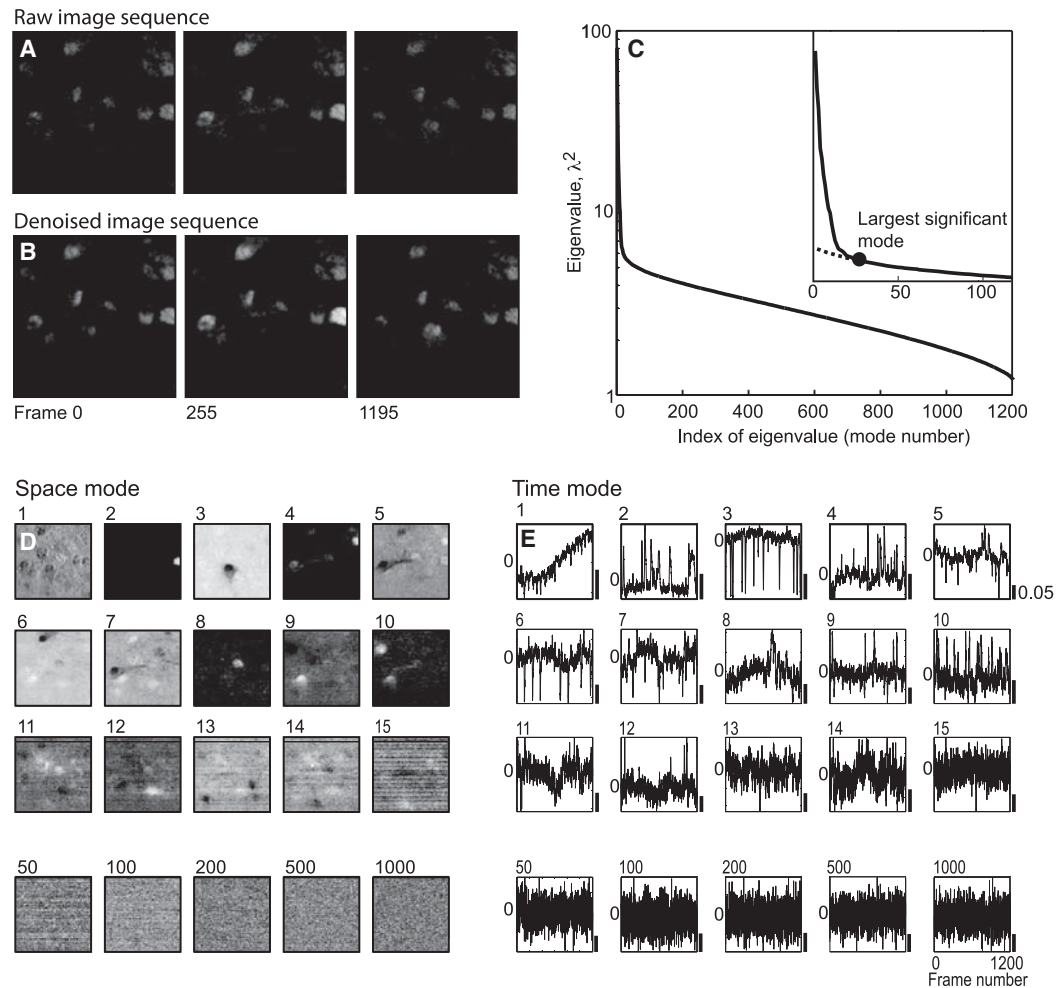
D. Kleinfeld and P.P. Mitra

FIGURE 4. Denoising of spinning-disk confocal imaging data on Ca^{2+} waves in organotypic culture. (*A*) Selected frames from a 1200-frame sequence of 100×100-pixel data. (*B*) The same data set after reconstruction with 25 of the 1200 modes (Equation 29). Denoising is particularly clear when the data are viewed as video clips. (*C*) Singular value decomposition of the imaging sequence in (*A*). The spectrum for the square of the eigenvalues for the space and time modes. Note the excess variance in the roughly 25 dominant modes (Equations 27 and 28). (*D*) The top 15 spatial modes, $F_n(s)$, plus high-order modes. Light shades correspond to positive values and dark shades negative values. The amplitude of the modes is set by the orthonormal condition $\sum_{t=1}^{N_t} F_m(t)F_n(t) = \delta_{nm}$. (*E*) The top 15 temporal modes of $G_n(t)$. The amplitude of the modes is set by the orthonormal condition $\sum_{t=1}^{N_t} G_m(t)G_n(t) = \delta_{nm}$ (JT Vogelstein, unpubl.). Fields in *A*, *B*, and *D* are 115 μm on edge.

where the rank of $V(s, t)$ is the smaller of the pixel or time dimensions. For example, data of Figure 4A, there are $N_t = 1200$ frames or time points and $N_s = 10,000$ pixels, so that rank$\{V(s, t)\} = N_t$. The above decomposition is referred to as a singular-value decomposition (Golub and Kahan 1965). The temporal functions satisfy an eigenvalue equation, that is,

$$\sum_{t'=1}^{N_t} G_n(t') \sum_{s=1}^{N_s} V(s, t)V(s, t') = \lambda_n^2 . G_n(t), \tag{27}$$

where the functions $F_n(s)$ and $G_n(t)$ are orthonormal. The spatial function that accompanies each temporal function is found by inverting the defining equation, so that

$$F_n(s) = \frac{1}{\lambda_n} \sum_{t=1}^{N_t} V(s, t) \, G_n(t). \tag{28}$$

For completeness, note that this is equivalent to determining the principal components of responses recorded from a single location across multiple trials, as opposed to multiple locations in a single trial, where s labels the trial rather than the location.

When this decomposition is applied to the Ca^{2+} imaging data (Fig. 4A), we see that the eigenvalue spectrum has large values for the low-order modes and then rapidly falls to a smoothly decreasing function of index (Fig. 4B); theoretical expressions for the baseline distribution have been derived (Sengupta and Mitra 1999). The spatial and temporal modes show defined structure for the first ~20 modes; beyond this the spatial modes appear increasingly "grainy" and the temporal modes appear as fast noise (Fig. 4D,E).

The utility of this decomposition is that only the lower-order modes carry information. Thus we can reconstruct the data matrix from only these modes and remove the "fast" noise, that is,

$$V^{\text{reconstructed}}(s,t) = \sum_{n=1}^{\substack{\text{largest significant mode}}} \lambda_n \, F_n(s) \, G_n(t). \tag{29}$$

Compared with smoothing techniques, the truncated reconstruction respects all correlated features in the data and thus, for example, does not remove sharp edges. Reconstruction of the intracellular Ca^{2+} oscillation data highlights the correlated activity by removing fast, grainy variability (Fig. 4B).

CASE FOUR: SPECTROGRAMS AND SPACE-FREQUENCY SINGULAR-VALUE DECOMPOSITION

The final example concerns the characterization of coherent spatiotemporal dynamics, such as waves of activity. We return to the use of voltage-sensitive dyes, this time to image the electrical dynamics of turtle visual cortex in response to a looming stimulus. Early work had shown that a looming stimulus led to the onset of ~20-Hz oscillations, the g-band for turtle, in visual cortex (Prechtl and Bullock 1994, 1995). The limited range of cortical connections led to the hypothesis that this oscillation might be part of wave motion. We investigated this issue by direct electrical measurements throughout the depth of cortex at selected sites (Prechtl et al. 2000) and, of relevance for the present discussion, by imaging the spatial patterns from cortex using voltage-sensitive dyes as the contrast agent (Prechtl et al. 1997).

The electrical activity is expected to evolve between prestimulus versus poststimulus epochs and possibly over an extended period of stimulation. Thus the spectral power is not stationary over long periods of time and we must consider a running measure of the spectral power density, denoted the spectrogram, that is a function of both frequency and time. We choose a restricted interval of time, denoted T_{window}, with N_{window} data points, compute the Fourier transforms $\tilde{V}^{(k)}(f;t_0)$, and spectrum $\tilde{S}(f;t_0)$ over that interval, where t_0 indexes the time at the middle of the epoch, and then step forward in time and recalculate the transforms and spectrum. Thus

$$\tilde{V}^{(k)}(f;t_0) = \frac{1}{\sqrt{N}} \sum_{t=t_0-(1/2)N_{\text{window}}}^{t_0+(1/2)N_{\text{window}}-1} e^{-i2\pi ft} \, w_t^{(k)} \, V_t \tag{30}$$

and

$$\tilde{S}(f;t_0) \equiv \frac{1}{K} \sum_{k=1}^{K} \left| \tilde{V}^{(k)}(f;t_0) \right|^2. \tag{31}$$

The resolution half-bandwidth is now p/N_{window} and, as a practical matter, the index is shifted in increments no larger than $N_{\text{window}}/2$. For the case of the summed optical signal from turtle cortex, we
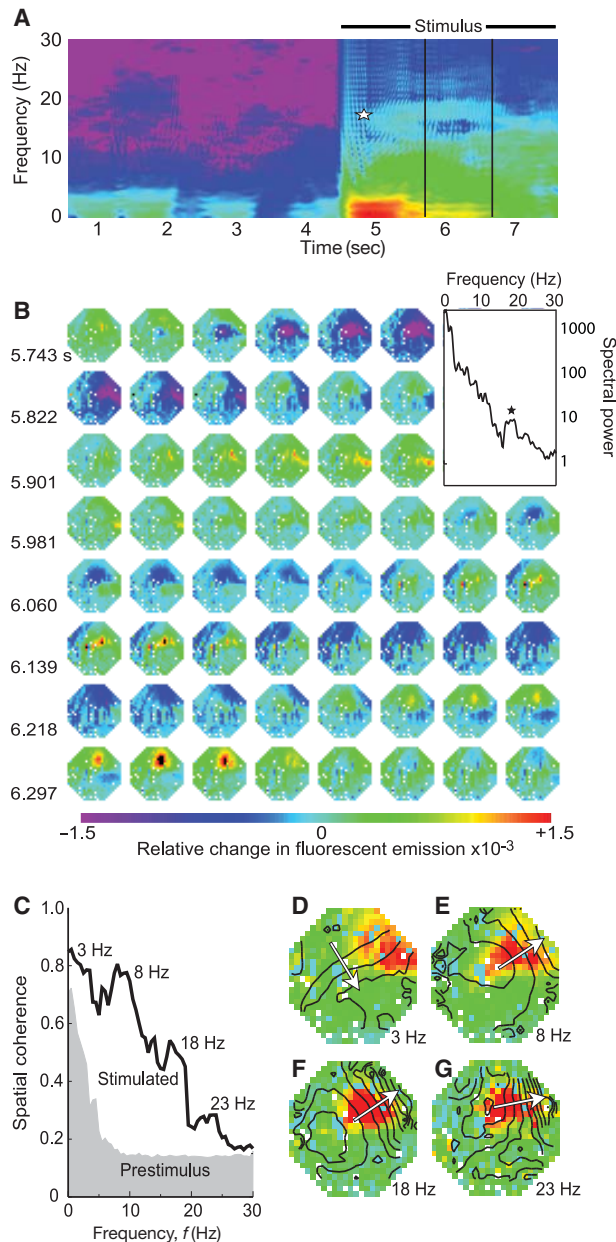
FIGURE 5. Analysis of single-trial voltage-sensitive dye imaging data to delineate collective excitation in visual cortex of turtle. (*A*) Spectrogram of the response averaged over all active pixels in the image (Equations 30 and 31). (*B*) Space–time response during the period when the animal was presented with a looming stimulus. The data were denoised (Equation 29), low-pass filtered at 60 Hz, and median filtered (400-msec width) to remove a stimulus-induced depolarization. We show every eighth frame (126 Hz); note the flow of depolarization from *left* to *right*. The *inset* is the spectrum for the interval 4.7–5.7 sec and is the power spectrum over the $T = 1$ sec interval that encompasses this epoch (black band in *A*). (*C*) Coherence, $\tilde{C}(f_0)$, over intervals both before and after the onset ($T = 3$ sec; $K = 7$) estimated at successive frequency bins; $\tilde{C}(f_0) > 0.14$ indicates significance (Equations 33–35). (*D–G*) Spatial distribution of amplitude (red for maximum and blue for zero) and phase ($\pi/12$ radians per contour; arrow indicates dominant gradient) of the coherence at $f_0 = 3$, 8, 18, and 22 Hz, respectively, during stimulation. Fields in *B* and *D–G* are 3.5 mm in diameter. (Modified from Prechtl et al. 1997.)

observe low-frequency activity before stimulation and multiple bands of high-frequency oscillations on stimulation (Fig. 5A). A particularly pronounced band occurs near 18 Hz; this is clearly seen in a line plot of the spectral power density for the 1-sec epoch centered in the middle of the stimulation period (inset in Fig. 5B).

Cite this introduction as *Cold Spring Harb Protoc*; doi:10.1101/pdb.top081075

The image data, even after denoising (Equation 29) and broad-band filtering, appears complex (Fig. 5B), with regions of net depolarization sweeping across cortex, but no simple pattern emerges. One possibility is that cortex supports multiple dynamic processes, each with a unique center frequency, that may be decomposed by a singular value decomposition in the frequency domain. In this method, proposed by Mann and Park (1994), the space–time data $V(s, t)$ is first projected into a local temporal frequency domain by transforming with respect to a set of tapers, that is,

$$\tilde{V}^{(k)}(s, f) = \frac{1}{\sqrt{N}} \sum_{t=1}^{N} e^{-i2\pi ft} \, w_t^{(k)} V_t(s). \tag{32}$$

The index k defines a local frequency index in the band $[f_0 - \Delta f/2, f_0 + \Delta f/2]$. For a fixed frequency, f_0, a SVD is performed on the complex matrix

$$\tilde{V}(s, k; f_0) \equiv \tilde{V}^{(1)}(s, f_0), \; \ldots \; , \tilde{V}^{(K)}(s, f_0) \tag{33}$$

to yield

$$\tilde{V}(s, k; f_0) = \sum_{n=1}^{\text{rank}\{\tilde{V}\}} \lambda_n \, \tilde{F}_n(s) \, \tilde{G}_n(k), \tag{34}$$

where the rank is invariably set by K. A measure of coherence is given by the ratio of the power of the leading mode to the total power (Fig. 5C), that is,

$$\tilde{C}(f_0) = \frac{\lambda_1^2(f_0)}{\sum_{k=1}^{K} \lambda_k^2(f_0)} . \tag{35}$$

A completely coherent response leads to $\tilde{C}(f_0) = 1$, whereas for a uniform random process $\tilde{C}(f_0) = 1/K$. Where $\tilde{C}(f_0)$ has a peak, it is useful to examine the largest spatial mode, $\tilde{F}_1(s)$. The magnitude of this complex image gives the spatial distribution of coherence that is centered at frequency f_0, whereas gradients in the phase of the image indicate the local direction of propagation.

For the example data (Fig. 5B), this analysis revealed linear waves as the dominant mode of electrical activity. Those with a temporal frequency centered at $f_0 = 3$ Hz are present with or without stimulation (Prechtl et al. 1997) (Fig. 5D), whereas those centered at $f_0 = 8$, 18, and 23 Hz are seen only with stimulation and propagate orthogonal to the wave at 3 Hz (Fig. 5E–G). It is of biological interest that the waves at $f_0 = 3$ Hz track the direction of thalamocortical input, whereas those at higher frequencies track a slight bias in axonal orientation (Cosans and Ulinski 1990) that was unappreciated in the original work (Prechtl et al. 1997).

CONCLUSION

This introduction covers a number of key applications of spectral methods to optical imaging data. The choice of topics is representative but by no means exhaustive. An additional application that is likely to be of utility is the fitting of line spectra to signals with relatively pure periodic contributions, such as may occur from physiological rhythms, from the response to a periodic stimulus, or from environmental contaminants like line power (Mitra et al. 1999; Pesaran et al. 2005). A second application of note is demodulation of a spatial image in response to periodic stimulation either at the fundamental drive frequency (Borst 1995; Kalatsky and Stryker 2003; Sornborger et al. 2005) or the second harmonic of the drive (Benucci et al. 2007). Demodulation also is valuable for delineating wave dynamics in systems with rhythmic activity (Kleinfeld et al. 1994; Prechtl et al. 1997). In general, spectral techniques are an essential tool for the statistical analysis of imaging data.

D. Kleinfeld and P.P. Mitra

ACKNOWLEDGMENTS

REFERENCES

Ahmed N, Rao KR. 1975. *Orthogonal transforms for digital signal processing.* Springer, New York.

Benucci A, Frazor RA, Carandini M. 2007. Standing waves and traveling waves distinguish two circuits in visual cortex. *Neuron* **55:** 103–117.

Borst A. 1995. Periodic current injection (PCI): A new method to image steady-state membrane potential of single neurons in situ using extracellular voltage-sensitive dyes. *Z Naturforsch* **50:** 435–438.

Cacciatore TW, Brodfueher PD, Gonzalez JE, Jiang T, Adams SR, Tsien RY, Kristan WB Jr, Kleinfeld D. 1999. Identification of neural circuits by imaging coherent electrical activity with FRET-based dyes. *Neuron* **23:** 449–459.

Cosans CE, Ulinski PS. 1990. Spatial organization of axons in turtle visual cortex: Intralamellar and interlamellar projections. *J Comp Neurol* **296:** 548–558.

Devor A, Tian P, Nishimura N, Teng IC, Hillman EM, Narayanan SN, Ulbert I, Boas DA, Kleinfeld D, Dale AM. 2007. Suppressed neuronal activity and concurrent arteriolar vasoconstriction may explain negative blood oxygenation level-dependent signaling. *J Neurosci* **27:** 4452–4459.

Golub GH, Kahan W. 1965. *Calculating singular values and pseudo-inverse of a matrix.* Society for Industrial and Applied Mathematics, Philadelphia.

Hannan EJ. 1970. *Multiple time series.* Wiley, New York.

Jarvis MR, Mitra PP. 2001. Sampling properties of the spectrum and coherency of sequences of action potentials. *Neural Comput* **13:** 717–749.

Kalatsky VA, Stryker MP. 2003. New paradigm for optical imaging: Temporally encoded maps of intrinsic signal. *Neuron* **38:** 529–545.

Kleinfeld D. 2008. Application of spectral methods to representative data sets in electrophysiology and functional neuroimaging. In *Syllabus for society for neuroscience short course III on "neural signal processing: Quantitative analysis of neural activity"* (ed. Mitra P), pp. 21–34. Society for Neuroscience, Washington, DC.

Kleinfeld D, Delaney KR, Fee MS, Flores JA, Tank DW, Gelperin A. 1994. Dynamics of propagating waves in the olfactory network of a terrestrial mollusk: An electrical and optical study. *J Neurophysiol* **72:** 1402–1419.

Kleinfeld D, Mitra PP, Helmchen F, Denk W. 1998. Fluctuations and stimulus-induced changes in blood flow observed in individual capillaries in layers 2 through 4 of rat neocortex. *Proc Natl Acad Sci* **95:** 15741–15746.

Mann ME, Park J. 1994. Global-scale modes of surface temperature variability on interannual to century timescales. *J Geophys Res* **99:** 25819–25833.

Mayhew JEW, Askew S, Zeng Y, Porrill J, Westby GWM, Redgrave P, Rector DM, Harper RM. 1996. Cerebral vasomotion: 0.1 Hz oscillation in reflectance imaging of neural activity. *Neuroimage* **4:** 183–193.

Mitra PP, Bokil HS. 2008. *Observed brain dynamics.* Oxford University Press, New York.

Mitra PP, Pesaran B. 1998. Analysis of dynamic brain imaging data. *Biophys J* **76:** 691–708.

Mitra PP, Pesaran B, Kleinfeld D. 1999. Analysis of dynamic optical imaging data. In *Imaging neurons: A laboratory manual* (ed. Yuste R, et al.),

pp. 9.1–9.9. Cold Spring Harbor Laboratory Press, Cold Spring Harbor, NY.

Nishimura B, Schaffer CB, Friedman B, Lyden PD, Kleinfeld D. 2007. Penetrating arterioles are a bottleneck in the perfusion of neocortex. *Proc Natl Acad Sci* **104:** 365–370.

Osol G, Halpern W. 1988. Spontaneous vasomotion in pressurized cerebral arteries from genetically hypertensive rats. *Am J Physiol* **254:** H28–H33.

Papoulis A. 1962. *The Fourier integral and its applications.* McGraw-Hill, New York.

Percival DB, Walden AT. 1993. *Spectral analysis for physical applications: Multitaper and conventional univariate techniques.* Cambridge University Press, Cambridge.

Pesaran B, Sornborger A, Nishimura N, Kleinfeld D, Mitra PP. 2005. Spectral analysis for dynamical imaging data. In *Imaging in neuroscience and development: A laboratory manual* (ed. Yuste R, Konnerth A), pp. 439–444. Cold Spring Harbor Laboratory Press, Cold Spring Harbor, NY.

Prechtl JC, Bullock TH. 1994. Event-related potentials to omitted visual stimuli in a reptile. *Electroencephal Clin Neurophys* **91:** 54–66.

Prechtl JC, Bullock TH. 1995. Structure and propagation of cortical oscillations linked to visual behaviors in the turtle. In *Proceedings of the 2nd joint symposium on neural computation* (ed. Sejnowski TJ), pp. 105–114. Institute for Neural Computation, University of California, San Diego and California Institute of Technology.

Prechtl JC, Cohen LB, Mitra PP, Pesaran B, Kleinfeld D. 1997. Visual stimuli induce waves of electrical activity in turtle cortex. *Proc Natl Acad Sci* **94:** 7621–7626.

Prechtl JC, Bullock TH, Kleinfeld D. 2000. Direct evidence for local oscillatory current sources and intracortical phase gradients in turtle visual cortex. *Proc Natl Acad Sci* **97:** 877–882.

Sengupta AM, Mitra PP. 1999. Distributions of singular values for some random matrices. *Phys Rev E* **60:** 3389–3392.

Shih AY, Friedman B, Drew PJ, Tsai PS, Lyden PD, Kleinfeld D. 2009. Active dilation of penetrating arterioles restores red blood cell flux to penumbral neocortex after focal stroke. *J Cerebr Blood Flow Metab* **29:** 738–751.

Sornborger A, Yokoo T, Delorme A, Sailstad C, Sirovich L. 2005. Extraction of the average and differential dynamical response in stimulus-locked experimental data. *J Neurosci Methods* **141:** 223–229.

Taylor AL, Cottrell GW, Kleinfeld D, Kristan WB. 2003. Imaging reveals synaptic targets of a swim-terminating neuron in the leech CNS. *J Neurosci* **23:** 11402–11410.

Thomson DJ. 1982. Spectral estimation and harmonic analysis. *Proc IEEE* **70:** 1055–1096.

Thomson DJ, Chave AD. 1991. Jackknifed error estimates for spectra, coherences, and transfer functions. In *Advances in spectrum analysis and array processing* (ed. Shykin S), pp. 58–113. Prentice Hall, Englewood Cliffs, NJ.

Cite this introduction as *Cold Spring Harb Protoc;* doi:10.1101/pdb.top081075